ACS Catalysis

pubs.acs.org/acscatalysis Research Article

Unraveling the Blessing and Curse of the IrCu Aerogel Catalyst for the Oxygen Evolution Reaction

Amir Gasmi,* Meryem Ennaji, Carlos A. Campos-Roldán, Morgane Stodel, Tristan Asset, Vasiliki Papaefthymiou, Andrea Zitolo, Marc Dupont, Frédéric Lecoeur, Jakub Drnec, Deborah Jones, and Raphaël Chattot*

Cite This: *ACS Catal.* 2026, 16, 4528−4540 Read Online

ACCESS | Metrics & More | Article Recommendations | Supporting Information

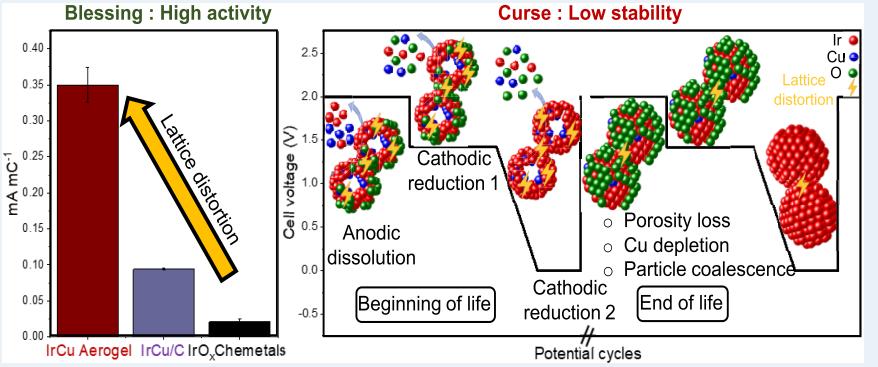

ABSTRACT: Improving the intrinsic activity and utilization of iridium (Ir)-based catalysts for the oxygen evolution reaction (OER) is essential to the market penetration of proton exchange membrane water electrolyzers (PEMWEs). However, conventional electronic structure modulation strategies relying on the introduction of transition metals through alloying and doping face serious stability issues. In this study, we examine the structure−activity−stability relationships toward the OER of an IrCu aerogel in comparison to dispersed IrCu nanoparticles and a commercial IrO_x benchmark. Using a combination of *ex situ*, *in situ*, and *post mortem* techniques, we show that the high OER activity of the IrCu aerogel originates primarily from the presence of lattice distortions, *i.e.*, through a structural effect rather than an alloying effect. Moreover, beyond decisively influencing the electrocatalytic activity, the structure is shown to inhibit the formation of stable Ir oxide species during operation unlike for isolated nanoparticles, which is detrimental to the aerogel stability during accelerated stress tests in PEMWE.

KEYWORDS: *lattice distortion, heterogeneous catalysis, PEM water electrolysis, oxygen evolution reaction, aerogel*

Downloaded via INIST-CNRS on March 27, 2026 at 14:32:52 (UTC).
See https://pubs.acs.org/sharingguidelines for options on how to legitimately share published articles.

INTRODUCTION

In the context of depleting fossil fuels, increasing greenhouse gas emissions, global warming, and concerns over resource sustainability, and the development of renewable energy vectors is of paramount importance.[1,2] Green hydrogen, generated *via* water electrolysis, offers a clean alternative to fossil fuels for energy storage and utilization.[2−8] Among the available technologies, proton exchange membrane water electrolysis (PEMWE) is particularly promising due to its high-power density, efficiency, and compact cell design.[9−11] However, the PEMWE anode operates under harsh oxidizing conditions, including low pH (<1), high potentials (up to 2 V *vs* the reversible hydrogen electrode, RHE), and high oxygen concentrations. This makes the selection of effective and stable electrocatalysts to enhance the limiting oxygen evolution reaction (OER) particularly challenging.[12] Unsupported iridium oxide (IrO_2) remains the state-of-the-art OER catalyst, owing to its high stability. However, its low surface area demands high Ir loadings to ensure sufficient active site availability for practical hydrogen production. Given the scarcity and cost of Ir, reducing its content from the current 2−3 mg_{Ir} cm^{-2} to around 0.25−0.4 mg_{Ir} cm^{-2} is essential for broader PEMWE adoption.[13,14] At such low loadings, however, state-of-the-art IrO_2 tends to form thin, noncontiguous catalytic layers with poor in-plane electronic conductivity and limited overall catalytic performance. Solving this bottleneck requires nanostructured catalyst layers.

Several approaches have been explored with this goal.[15−19] A general strategy employs supports that enable the dispersion of

Received: October 30, 2025
Revised: January 27, 2026
Accepted: January 28, 2026
Published: February 12, 2026

© 2026 The Authors. Published by American Chemical Society

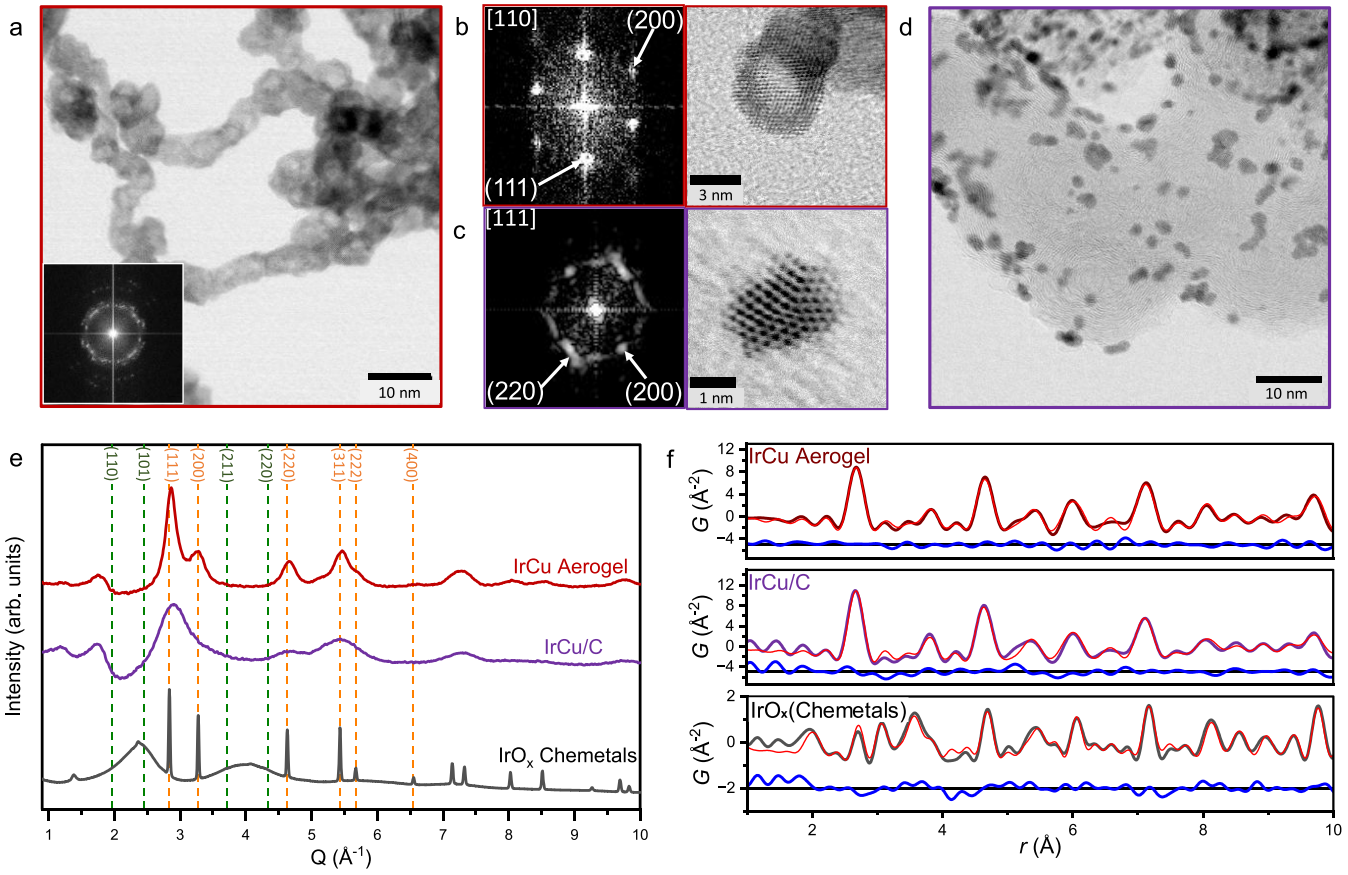

Figure 1. *Ex situ* morphological and structural characterization of IrCu aerogel, IrCu/C, and IrO_x Chemetals. (a, d) HR-TEM of IrCu aerogel and IrCu/C, respectively. The insets in panel (a) correspond to the fast Fourier transform (FFT) of several building units of the aerogel. (b, c) HR-TEM images with corresponding FFT for the IrCu aerogel building units and single IrCu/C nanoparticle. (e) TS patterns comparing IrCu catalysts and IrO_x Chemetals. The green dotted lines indicate diffraction peak positions corresponding to the IrO_2 rutile phase, while the orange dotted lines highlight peak positions associated with the Ir fcc metallic phase. (f) *Ex situ* reduced pair distribution function $G(r)$ profiles and corresponding fits (in red) for IrCu aerogel (top), IrCu/C (middle), and IrO_x Chemetals (bottom). The residuals (difference between experimental and calculated data) are shown in blue beneath each curve with the zero-reference line in black.

small Ir-based nanoparticles (NPs) with a high surface-to-volume ratio, thereby enhancing catalytic activity while reducing the amount of Ir required.[20,21] Although carbon is an ideal support due to its high conductivity and surface area, it degrades rapidly under PEMWE anode conditions. Consequently, metal oxide supports have been considered. However, their semiconductor nature necessitates atomic doping to improve their electronic conductivity. Niobium-, antimony-, fluorine-, indium-, and tantalum-doped tin oxide (SnO_2) have therefore received considerable attention.[22−] Although doping can initially improve conductivity, this effect may diminish over time due to dopant leaching.[30,31] In fact, higher conductivity is achieved in metal-oxide-supported Ir when a percolated IrO_2 network forms.[32] Pushing this reasoning further, metal aerogels have emerged as promising candidate. Their self-supported, percolated network provides a high specific surface area and volumetric mass density, allowing for conformal catalyst layers even at low loadings.

Shi et al. reported the successful synthesis of an IrCu aerogel and attributed its high OER activity in liquid electrolyte to a combination of optimized binding energy of Ir with oxygen intermediates by alloying Ir with an appropriate amount of Cu (Ir:Cu = 3 according to first principle calculations), and the large number of active sites provided by the highly porous aerogel structure.[32] However, the notorious instability of surface Cu under the OER conditions raises questions about this interpretation of the observed catalytic improvement. In fact, the branched structure of metal aerogels features a high density of grain boundaries between the building units of the network.[33] At grain boundaries, local variations in coordination[34−36] and lattice distortion (microstrain)[37−42] are known to strongly impact heterogeneous (electro)catalysis properties.[43] For the oxygen reduction reaction (ORR), several studies have demonstrated their impact on activity, particularly in liquid electrolytes.[37−3839,44,] However, such local structure−activity relationships remain largely unexplored for the OER.[46]

In this contribution, an IrCu aerogel and carbon-supported IrCu/C nanoparticles were synthesized, and their OER activities were compared with those of an IrO_x benchmark (Surepure Chemetals). Particularly, the influence of the materials' physicochemical properties on their electrocatalytic activity for the OER is investigated throughout different key stages of the catalyst lifecycle (*viz.*, the as-prepared precatalyst, after electrochemical activation and at its end-of-life) in liquid electrolyte, using *ex situ*, *in situ*, and *post mortem* techniques, including high-resolution transmission electron microscopy (HRTEM), X-ray photoelectron spectroscopy (XPS), electrochemical online inductively coupled plasma mass spectrometry (ICP-MS), extended X-ray absorption fine structure (EXAFS), high energy X-ray total scattering (TS) coupled with pair

https://doi.org/10.1021/acscatal.5c07713
ACS Catal. 2026, 16, 4528−4540

Table 1. Microstructural Parameters and Chemical Composition of the As-Prepared Precatalysts from *Ex Situ* TS-PDF

	TS-PDF							
	fcc metal phase				rutile oxide phase			
sample	a (Å)	size (nm)	$U_{iso} \times 10^4$ (Å^2)	wt (%)	$a = b$, c (Å)	size (nm)	$U_{iso} \times 10^4$ (Å^2)	R_w
IrCu aerogel	3.748	2.5	54	100				0.18
IrCu/C	3.721	1.60	45	100				0.24
IrO_x Chemetals	3.814	20[a]	9	7	4.649, 3.083	0.8	73	0.48

[a]This size corresponds to the longest pair distance present in the PDF and was not refined.

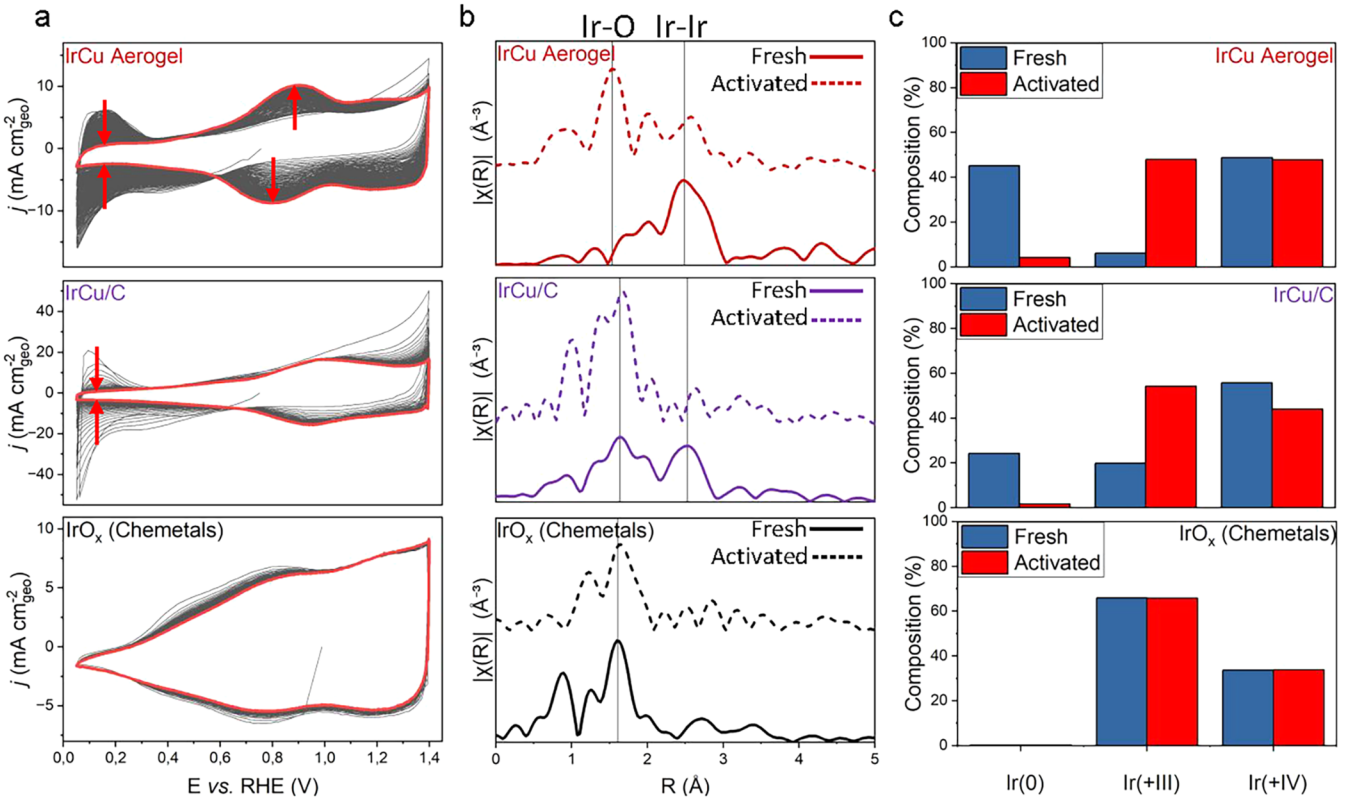

Figure 2. Electrochemical activation in 1 M HClO4 and structural−chemical evolution of IrCu aerogel, IrCu/C, and IrO_x Chemetals. (a) Cyclic voltammograms (CV) recorded during electrochemical activation; the red line corresponds to the final stable CV and the red arrows indicate the evolution of characteristic peaks. (b) Ir L3-edge FT-EXAFS (not phase-shift corrected) spectra before and after activation. (c) Ir oxidation state distributions derived from XPS before and after activation.

distribution function (PDF) analysis, and the Rietveld methods. The observed structural, chemical, and morphological changes were then correlated with the OER activity and stability measured in both liquid and PEMWE single-cell configurations. Overall, the results show a rapid and substantial dissolution of Cu from the IrCu alloys at the early stage of catalyst activation, highlighting the primacy of the remaining lattice distortion in controlling the activity of the IrCu aerogel over alloying effects. Moreover, beyond influencing the electrocatalytic activity, the aerogel structure is shown to inhibit the formation of stable electrochemical Ir oxides during electrochemical activation, in contrast to the isolated nanoparticles (IrCu/C). This is detrimental to aerogel stability in PEMWE, particularly during accelerated stress tests (ASTs), simulating intermittent PEMWE operation. This calls for a further stabilization of the aerogel structure at the synthesis or postsynthesis stage.

RESULTS AND DISCUSSION

The IrCu aerogel was synthesized following a protocol inspired by Shi et al.,[32] *via* chemical reduction of iridium and copper salts (3:1 molar ratio) using sodium borohydride ($NaBH_4$), as a reducing agent, at 60 °C (see Materials and Methods). For comparison, IrCu nanoparticles with a similar Ir/Cu molar ratio were synthesized using a protocol inspired by Bornet et al.,[47] using basic ethanol as a solvent, reducing agent, and stabilizer, yielding nanoparticles in colloidal suspension that were subsequently deposited onto Vulcan XC-72R carbon support (Cabot), resulting in a final Ir loading of 23 wt % (see Materials and Methods). Note that carbon was chosen as support over metal oxide to facilitate characterization of the nanoparticles composing the IrCu/C catalyst by means of X-ray scattering, but its instability in the OER conditions is considered in the following. HR-TEM images (Figure 1a,b) confirm that, as for Shi et al.,[32] the IrCu aerogel is highly nanostructured, being composed of a porous, interconnected network of hollow nanoparticles featuring a ∼1 nm thick shell

https://doi.org/10.1021/acscatal.5c07713
ACS Catal. 2026, 16, 4528−4540

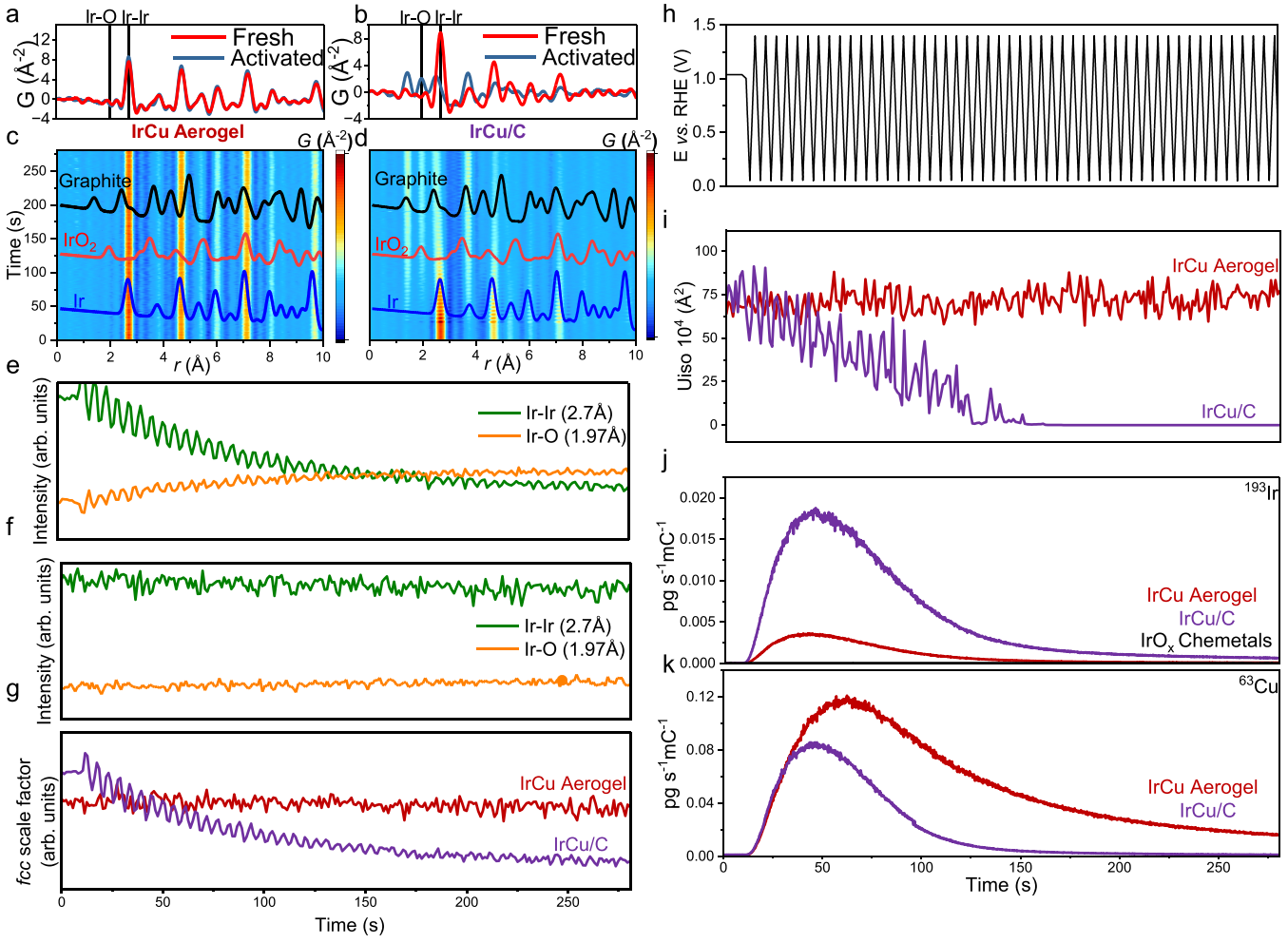

Figure 3. Microstructural and chemical evolution of IrCu aerogel and IrCu/C during electrochemical activation in 1 M $HClO_4$. (a, b) *In situ* pair distribution function (PDF) $G(r)$ patterns collected before (fresh) and after activation for (a) IrCu aerogel and (b) IrCu/C. *In situ* PDF $G(r)$ waterfall plots for (c) IrCu aerogel and (d) IrCu/C over time, with calculated PDFs of graphite (black), rutile IrO_2 (red), and metallic Ir (blue) overlaid as references. Selected time-resolved PDFs showing the evolution of Ir−Ir (2.7 Å) and Ir−O (1.97 Å) peaks for (e) IrCu aerogel and (f) IrCu/C. (g) Evolution of the fcc scale factor extracted from PDF fitting. (h) Applied potential profile (*E vs* RHE) during electrochemical activation. (i) Time-dependent evolution of U_{iso} parameter. (j, k) Specific Ir and Cu dissolution profiles during the electrochemical activation for IrCu aerogel, IrCu/C and IrO_x Chemetals catalysts.

of approximately ∼5 nm external diameter. In contrast, the IrCu/C catalyst (Figure 1c,d) features dispersed nanoparticles of ∼1.5 nm on the carbon support. Consequently, both IrCu aerogel and IrCu/C materials share a common size dimension (shell thickness and particle size, respectively) within two different crystal morphologies. The fast Fourier transform (FFT) of a single aerogel building unit (Figure 1b) displays distinct and well-defined diffraction spots, confirming its single crystalline nature. The observed reflections correspond to the (111) and (200) lattice planes, consistent with a face-centered cubic (fcc) structure viewed along the [110] zone axis. For an IrCu/C nanoparticle (Figure 1c), the FFT shows diffuse and multiple lattice points. This suggests crystal twinning, as evidenced by Pittkowski et al., on Ir/C nanoparticles prepared in a similar fashion.[48] In this case, reflections from the (220) and (200) lattice planes are observed along the [111] zone axis. Finally, FFT over larger aerogel areas (inset of Figure 1a) confirms its overall polycrystalline nature (observation of Debye−Scherrer rings). Bulk compositions determined by ICP-MS (see Table S1) show only little Cu retention in both materials after synthesis, with final Cu contents of 7.7 atom % in IrCu/C and 5 atom % in the aerogel, despite the initial Ir/Cu atomic ratio of 3:1. The microstructure of the as-prepared materials was further characterized by *ex situ* TS, first employing the Rietveld refinement method to extract crystallite size, lattice parameter, and microstrain values (see Table S1). As shown in Figure 1e, all TS patterns show the contribution of a fcc structure, pointing to either IrCu alloy formation for the synthesized catalyst and the presence of a metallic Ir phase in the IrO_x benchmark. Crystallite size of the fcc phases is approximately 3 nm for the aerogel, 0.9 nm for IrCu/C, and 22 nm for the IrO_x benchmark, in line with the particle sizes observed by TEM (Figures 1a,d and S1). The microstrain parameter suggests increasing lattice distortion content within the fcc phases, in the order: IrO_x Chemetals < IrCu/C < IrCu aerogel, with microstrain values of 1.3, 48, and 217%%, respectively (%% means the value is multiplied by 10^4). However, the broad peaks visible in the TS pattern of the IrO_x Chemetals sample in Figure 1e clearly suggest the presence of one or several additional and poorly crystalline phase(s). Consequently, the PDF method was used on TS data for further characterization of the local structure(s) comprising the

https://doi.org/10.1021/acscatal.5c07713
ACS Catal. 2026, 16, 4528−4540

samples. As shown in Figure 1f and in Table 1, a single fcc phase allowed us to accurately model the experimental PDFs of the two IrCu samples, in which no typical Ir−O pair distance of ∼2 Å is detected. However, the IrO_x Chemetals sample is found to be composed of ∼93 wt % highly amorphous rutile-like IrO_2 short-range domains (0.8 nm), with only a trace fraction of fcc metal Ir with large domains (∼20 nm). The coherent domain sizes of the IrCu fcc phases obtained by refining the PDFs were 2.5 and 1.60 nm for aerogel IrCu and IrCu/C, respectively, in relatively good agreement with the Rietveld method. Interestingly, the atomic mean square displacement amplitudes averaged over all directions (U_{iso}) for the different samples (fcc phases) increase in the following order: IrO_x Chemetals < IrCu/C < IrCu aerogel, as for the microstrain values. U_{iso} quantifies how much atoms deviate from their average positions due to thermal motion and/or static disorder; a higher U_{iso} indicates greater local disorder.

Contrary to the "bulk" PDF analysis, surface-sensitive XPS ("Fresh" traces in Figures 2c and S2) reveals that both IrCu materials do not contain only metallic Ir(0). In fact, both materials also show near-surface oxidation states corresponding to Ir(+III) and Ir(+IV), indicative of partial oxidation in air under ambient conditions. In contrast, the IrO_x benchmark contains no detectable metallic Ir(0) at the near surface. From combined PDF and XPS results, it can be concluded that the two IrCu materials are mainly metallic, with only a thin/partial layer of surface oxides. Ir L_3-edge EXAFS spectra were acquired for further comparison with PDF analysis. As shown in Figure 2b ("Fresh" traces), the Fourier transform (FT) EXAFS spectra shows largely dominant Ir−Ir contribution (∼2.5 Å) for IrCu aerogel and Ir−O contribution (∼1.5 Å) for IrO_x Chemetals, in good agreement with the results from PDFs. For IrCu/C, and contrary to PDF, EXAFS results show mixed contributions of Ir−O and Ir−Ir, in agreement with XPS showing a lower contribution of Ir(0) compared to that of the aerogel.

Prior to any catalytic activity measurement, all synthesized precatalysts were electrochemically activated through fast potential cycling (100 cycles) at 0.5 V s^{-1} between 0.05 and 1.4 V *vs* RHE in N_2 saturated 1 M $HClO_4$ until a stable surface state (the actual catalysts) was obtained. The structural evolution of the IrCu aerogel, IrCu/C nanoparticles, and IrO_x Chemetals before and after electrochemical activation is shown in Figure 2 through cyclic voltammograms (CVs), *ex situ* FT-EXAFS, and XPS. The IrCu aerogel initially displays clear redox peaks below 0.4 V *vs* RHE, usually associated with hydrogen underpotential deposition (H_{UPD}) process, indicating the presence of metallic Ir at the surface. Upon cycling between 0.05 and 1.4 V *vs* RHE, these H_{UPD} features progressively decrease, and are replaced by a redox couple at ∼0.9 V *vs* RHE, assigned to the reversible Ir(+III)/Ir(+IV) transition characteristic of hydrated Ir oxides.[49] Both the FT-EXAFS spectra in Figure 2b and XPS in Figures 2c and S2 ("Activated" traces) support this interpretation, with the appearance of Ir−O contribution (∼1.5 Å), and a shift of oxidation states from 45% Ir(0) and 48% Ir(+IV) to a mixture dominated by Ir(+III) and Ir(+IV) species, with only ∼5% remains as metallic Ir(0). Regarding the IrCu/C catalyst, the initial H_{UPD} features also vanish, while the FT-EXAFS spectrum is dominated by the Ir−O peak and XPS by Ir(+III) and Ir(+IV) species, with only ∼2% remaining as metallic Ir(0). The IrO_x Chemetals catalyst, in contrast, begins and remains predominantly oxidized throughout the process with a stable initial CV without any H_{UPD} features, accompanied by steady FT-EXAFS and XPS consistently showing dominant Ir−O coordination and mixed Ir(+III) and Ir(+IV) species. Overall, the three initially distinct surfaces of the precatalysts tend to a rather uniform oxidized state after electrochemical activation.

For more global insights into the electrocatalyst structures and chemical composition, the electrochemical activation was followed by *in situ* TS-PDF and online ICP-MS (see Supporting Information). Figure 3a,b displays the *in situ* PDFs obtained before and after electrochemical activation for both IrCu catalysts. In addition, waterfall plots of the IrCu aerogel (Figure 3c) and IrCu/C (Figure 3d) recorded during electrochemical activation are shown, with calculated PDFs of graphite (black), rutile IrO_2 (red), and metallic Ir (blue) overlaid for comparison. In the case of IrCu/C, we observe that while cycling, a new pair distance of ∼2 Å appears which is attributed to Ir−O. The rise of this peak is quantitatively plotted as a function of time in Figure 3f. Simultaneously, the probability of finding Ir−Ir distances decreases sharply. This indicates the formation of a short-range amorphous oxide phase (first Ir−O distance) which agrees with results from FT-EXAFS and XPS. In addition, peaks around ∼1.4 Å also appear after a few cycles, which can be assigned to graphitized regions of the carbon support, becoming visible as the strong signal from Ir−Ir pairs vanishes.[48] In contrast, the aerogel shows different behavior, with no new atomic pair distance appearing during electrochemical activation. As shown in Figure 3e, the probability to find Ir−Ir distances remains largely unchanged and the probability to find Ir−O remains absent all along the activation phase. This suggests that the aerogel remains to a large extent metallic, with the formation of surface oxides that cannot be detected using PDF. It must be noted at this stage that the high surface-to-volume ratio of the IrCu aerogel provided by its small crystallite size (∼2.5 nm) should, in principle, make surface contributions quite visible. In fact, and as further confirmed in parallel by the Rietveld refinement of the TS patterns (Figure S3), the microstructure (scattered intensity, lattice constant, and microstrain) of the fcc phase is found to respond dynamically with the applied electrode potential. As demonstrated in previous contributions,[50,51] this showcases the high sensitivity of the XRD technique to detect surface processes (adsorption, oxidation). To obtain quantitative insights, the PDFs were fitted using an fcc Ir unit cell model (see Supporting Information). As shown in Figure 3g, the fcc scale factor decreases over time for the IrCu/C catalyst while it remains essentially unchanged for the IrCu aerogel, in agreement with the formation of a new oxide phase in the former. The U_{iso} parameter, shown in Figure 3i, starts at comparable values for both catalysts but evolves differently: the U_{iso} for the aerogel remains relatively stable throughout the activation, whereas the U_{iso} for IrCu/C rapidly decreases to near zero (until not further refinable). This suggests that after electrochemical activation, the surfaces of both IrCu catalysts evolve toward an oxide state dominated by Ir(+III/+IV) species. However, the extent of oxidation differs significantly, with a much higher degree observed in IrCu/C. In contrast, the evolution of local lattice distortion follows a different trend, leading to a more defective structure in the aerogel compared to that in IrCu/C.

The specific metal dissolution rates measured by electrochemical online ICP-MS during activation are listed in Figure 3j,k. The IrO_x from Chemetals shows a low intensity Ir

https://doi.org/10.1021/acscatal.5c07713
ACS Catal. 2026, 16, 4528−4540

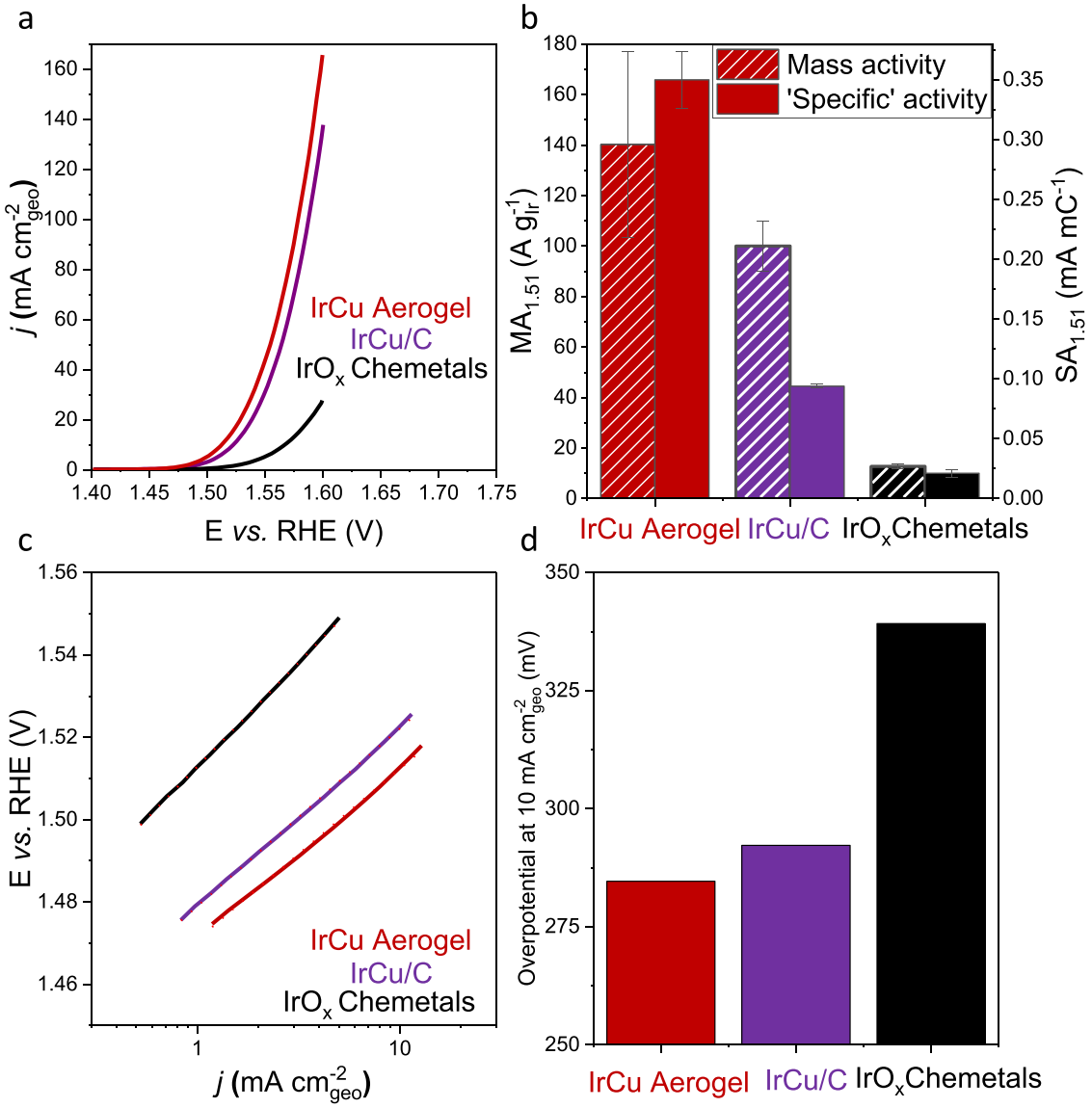

Figure 4. OER electrocatalytic performance in 1 M $HClO_4$. (a) Linear sweep voltammetry (LSV) curves recorded at a scan rate of 5 mV s^{-1}. (b) Mass and "specific" activities obtained at 1.51 V *vs* RHE. (c) Tafel plots (red dotted line corresponds to the linear fit) and (d) overpotential calculated at 10 mA cm^{-2}.

dissolution peak due to its initially oxidized/passivated surface, while the IrCu catalysts have higher dissolution rates. The IrCu/C nanoparticles exhibit a higher Ir dissolution rate than the aerogel, likely due to their smaller size, which makes them more prone to dissolution and/or detachment from the carbon support. The dissolution profiles were further resolved using a slower scan rate of 5 mV s^{-1} (Figure S4). The results confirm the stability of the benchmark catalyst, evidenced by a very low dissolution signal; a small cathodic peak appears only during reduction of preformed oxides. In contrast, the IrCu catalysts exhibit two Ir-related peaks: a dominant peak at higher potential (~1.40 V *vs* RHE), likely arising from overlapping anodic and cathodic dissolution associated with oxygen adsorption/desorption on Ir sites and a smaller peak at low potential (~0.05 V *vs* RHE) attributable to the reduction of residual oxides.[52]

Regarding the Cu dissolution, the integration of the dissolution profiles at the contact peak (dissolution due to the first contact of the catalyst with acid, see Figure S5) and the electrochemical activation shows that there is a pronounced change in the atomic composition of the catalysts, with the Cu atomic percentage decreasing from 7.7 to 4.3% for the supported particles and from 5 to 3.5% for the aerogel (Figure S6). Thus, the activated catalysts have a similar yet lower Cu content. It is noteworthy that complementary XPS measurements performed after electrochemical activation do not show detectable surface Cu (Figure S7). This confirms the high instability of Cu in OER conditions, and rules out the possibility for Cu to effectively tune the Ir binding energy with oxygen intermediates, even less with the optimal atomic fraction of Ir:Cu = 3 suggested by Shi et al.[32] Interestingly, and in contrast with the IrCu/C catalyst, both PDF analysis and the Rietveld method reveal the retention of atomic disorder (through the U_{iso} and microstrain parameters, respectively) over the course of electrochemical activation for the IrCu aerogel (Figures 3i and S3a).

After electrochemical activation, the catalytic activity of the different catalysts toward the OER was evaluated in N_2-

https://doi.org/10.1021/acscatal.5c07713
ACS Catal. 2026, 16, 4528−4540

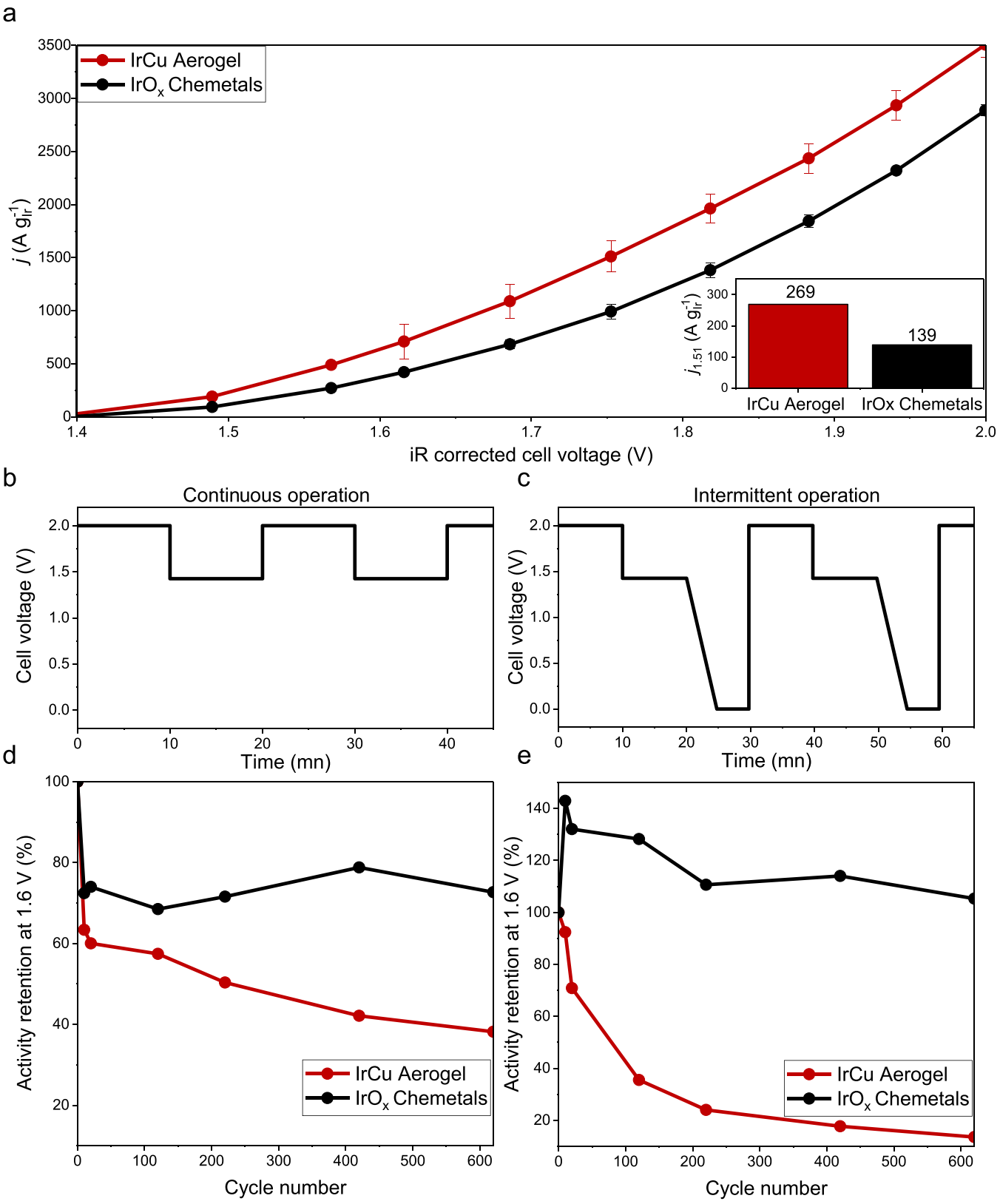

Figure 5. Electrocatalytic performance and durability of IrCu aerogel and IrO_x Chemetals in PEMWE. (a) Polarization curves with insets showing mass activities at 1.51 V. Potential profiles of (b) continuous and (c) intermittent PEMWE operation. (d, e) Corresponding activity retention at 1.6 V for (b) and (c), respectively.

saturated 1 M $HClO_4$ at room temperature with a fixed iridium loading of 50 μg_{Ir} cm^{-2} (see Supporting Information). Figure 4a presents the *iR*-corrected OER polarization curves, normalized to the geometric area of the electrode, for the IrCu catalysts benchmarked against the IrO_x Chemetals. The corresponding mass-normalized and charge-normalized OER

https://doi.org/10.1021/acscatal.5c07713
ACS Catal. 2026, 16, 4528−4540

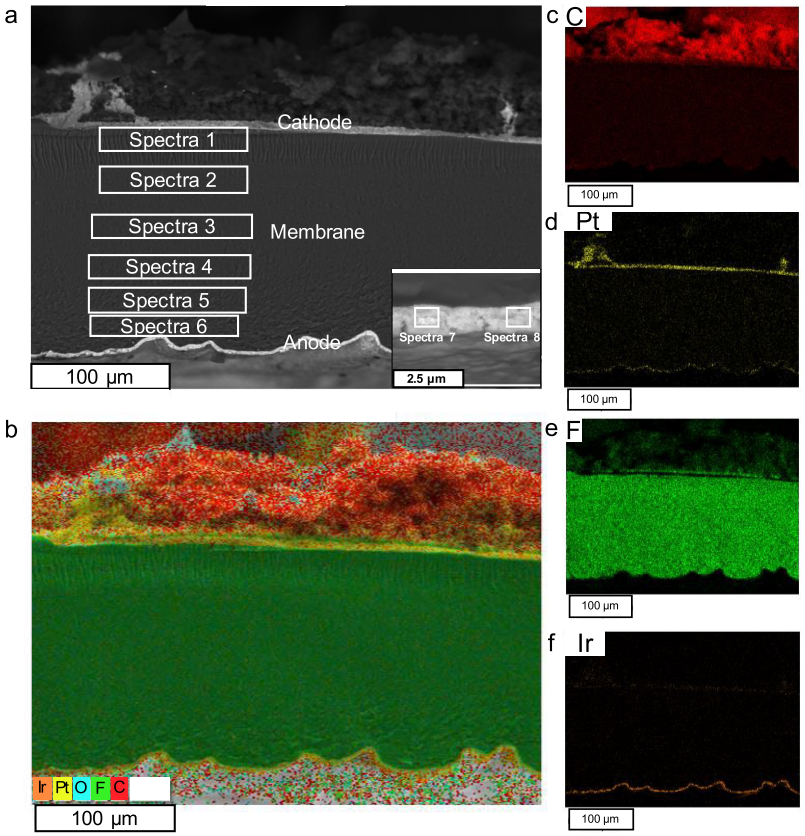

Figure 6. *Post mortem* cross-sectional EDX−SEM analysis of the MEA after continuous AST. (a) SEM image of the MEA cross section, indicating the cathode, membrane, and anode; the inset shows a magnified view of the anode catalyst layer with selected EDX acquisition regions. (b) Composite EDX elemental map of the MEA cross. Individual EDX elemental maps showing the distribution of (c) carbon (C), (d) platinum (Pt), (e) fluorine (F), and (f) iridium (Ir). Scale bars are indicated in each panel.

activities at 1.51 V *vs* RHE are shown in Figure 4b. To attempt a surface normalization, the surface was approximated by the electrochemical charge under the CV in the potential range of 0.4−1.4 V *vs* RHE in N_2-saturated 1 M $HClO_4$, as used in other studies.[26,53] Among the investigated materials, the IrCu aerogel exhibits the highest "specific" activity (0.35 mA mC^{-1}), corresponding to enhancements of approximately 4-fold and 17-fold relative to IrCu/C and IrO_x Chemetals, respectively. Similarly, the aerogel demonstrates the highest mass activity (140 A g_{Ir}^{-1}), marking an improvement of approximately 1.5-fold and 11-fold compared to IrCu/C and IrO_x Chemetals, respectively. The *iR*-free Tafel plots derived from the polarization curves (Figure 4c) further confirm the faster OER kinetics of the aerogel, which displays the lowest Tafel slope (45 mV dec^{-1}), indicative of more favorable reaction kinetics compared to IrCu/C (50 mV dec^{-1}) and IrO_x Chemetals (54 mV dec^{-1}). Additionally, the aerogel presents the lowest overpotential required to reach a current density of 10 mA cm^{-2} (Figure 4d), further confirming its enhanced performance. From all of the structural and chemical characterization described above, the high intrinsic activity of the IrCu aerogel is attributed to its high density of structural defects, which can modulate the adsorption energy of reaction intermediates on the catalyst surface,[39] also facilitating the formation of hydroxylated Ir species that have been reported to exhibit higher electrocatalytic activity.[48,54] In contrast, the effects of global strain and/or ligand (chemical effects), as reported in the previous study by Shi et al.,[32] appear negligible due to the instability of the alloying element (Cu) and its rapid dissolution under electrochemical conditions.

Catalyst powders of IrCu aerogel and IrO_x Chemetals were integrated into membrane electrode assemblies (MEAs) with an Ir loading of around 0.4 mg_{Ir} cm^{-2} at the anode using Nafion NRE-115 membranes and commercial 0.5 mg_{Pt} cm^{-2} gas diffusion electrodes (GDEs, Baltic FuelCells) at the cathode (see Supporting Information). The IrCu/C catalyst was not tested in PEMWE due to the instability of the carbon support.

The MEA break-in (activation) in PEMWE consisted of applying a constant potential at 1.6 V for a duration of 1 h. The PEMWE was operated at 80 °C with a MQ water flow of 200 mL h^{-1}. As presented in Figure 5a, the activity trends obtained in PEMWE qualitatively agree with results obtained in 1 M $HClO_4$ electrolyte at 25 °C, with the aerogel maintaining a higher activity compared to the benchmark. However, the enhancement factor of the aerogel compared to IrO_x Chemetals is decreased to less than 2-fold at 1.6 V (inset in Figure 5a). This can be attributed to the differences between the favorable conditions of a liquid cell, featuring a very thin catalyst layer immersed in a liquid electrolyte, and the more complex environment of MEAs, where the catalyst layer is significantly thicker and includes a solid electrolyte. This structural difference can introduce challenges related to the triple-phase boundary, where electrons, ions, and reactants must simultaneously interact for effective electrochemical reactions.[55,56] As a result, achieving high performance in such configurations requires not only a continuous and

https://doi.org/10.1021/acscatal.5c07713
ACS Catal. 2026, 16, 4528−4540

conductive catalyst network to facilitate in-plane electronic transport[57] but also a homogeneous distribution of ionomer throughout the layer to ensure efficient through-plane ionic conduction. The balance between these parameters is critical and must be carefully tailored to the specific properties and morphology of each catalyst system.

Finally, two different accelerated stress tests (ASTs) were conducted to evaluate catalyst stability under conditions simulating both continuous and intermittent PEMWE operation (Figure 5b,c). The continuous AST involved cycling between 1.426 and 2 V, while the intermittent AST included an additional excursion to 0 V for 5 min to simulate the low open-circuit voltage (OCV) reached in real systems in the presence of H_2 crossover from cathode to anode. The activity retention measured at 1.6 V is shown in Figure 5d,e for continuous and intermittent operation, respectively. The aerogel exhibits significant degradation, losing approximately 60% of its initial activity after 620 cycles in continuous mode and nearly 90% in intermittent mode. To obtain quantitative metrics for stability and enable comparison between the different catalysts, the *S*-number, as introduced by Geiger et al.,[58] was calculated at 1.51 V *vs* RHE (Figure S8). The results further confirm the lower stability of the IrCu aerogel compared with the benchmark catalyst, as evidenced by its smaller *S*-number value.

The lower stability of the aerogel comparing to the IrO_x chemetals is in agreement with those from characterization techniques including online ICP-MS, TS, XPS, and EXAFS as well as previous studies,[53,59] where the formation of an active Ir(+III/+IV) surface, predominantly composed of unstable amorphous hydroxyl species, prevents passivation of the catalyst, resulting in an accelerated dissolution rate, particularly upon returning to lower potentials (0 V excursion) which was observed during ICP-MS measurement through an additional dissolution peak appearing around 0 V (Figure S4).

To further investigate the origin of the low stability, cross-sectional energy-dispersive X-ray (EDX) mapping using scanning electron microscopy (SEM) was performed on an aged MEA after AST (continuous operation). In addition, elemental EDX analysis was conducted in different regions of the membrane and within the anode catalyst layer to assess the potential for membrane contamination by Cu or Cu migration through the membrane toward the cathode. The results, shown in Figure 6 and Table S2, indicate that Cu is detected only in the anode catalyst layer, at approximately 3 atom % relative to Ir, which is consistent with the initial Cu content of ∼5 atom %. These findings suggest that Cu dissolution is not the primary deactivation mechanism in this material. However, in general, and particularly for catalysts with higher transition-metal contents, metal dissolution can lead to membrane contamination or crossover to the cathode, thereby limiting the hydrogen evolution reaction, as reported in the literature. Consequently, chemical dealloying treatments such as acid washing may be beneficial for future nanoalloy OER catalysts to mitigate this potential degradation pathway, even though it does not appear to be dominant for the present material. To get a closer look on the node catalyst layer, *post mortem* HRTEM showed a significant morphological change during the intermittent AST compared to the continuous one, with a partial collapse of the aerogel structure and associated loss of surface area (Figure S9).

In contrast, the commercial benchmark catalyst exhibits negligible structural changes during the initial electrochemical activation step, showing a fully oxidized surface with a limited dissolution rate with a high stability number (on the order of 10^6). This results in superior stability under the continuous AST, retaining ∼70% of its initial activity after 620 cycles. Interestingly, under intermittent conditions, the commercial catalyst initially gains activity within the first 10 cycles before experiencing a decline, ultimately stabilizing at its initial activity. This behavior could be attributed to the transient reduction of Ir(+IV) to the more active Ir(+III) state induced by the 0 V excursions in the early cycles, a phenomenon also observed by Weiß et al.[60]

CONCLUSIONS

Local lattice distortion, rather than alloying effects, plays a primary role in enhancing activity toward the oxygen evolution reaction in IrCu aerogel catalyst, while Cu itself acts as a sacrificial agent to create porosity and defects during the synthesis stage. The IrCu aerogel exhibits a high intrinsic activity associated with pronounced microstrain within its structure. *In situ* X-ray total scattering with PDF analysis and Rietveld refinement confirms that these distortions persist under electrochemical conditions, potentially compensating for the inevitable loss of alloying effects (global strain and ligand) resulting from Cu dissolution. However, this enhanced activity is accompanied by a notable trade-off in durability, primarily driven by Ir dissolution under electrochemical stress stemming from the absence of a stable passivating oxide layer on the catalyst surface. Although this proof of concept is demonstrated using a catalyst with promising activity yet moderate stability, it calls for further optimization, notably by finding strategies to preoxidize the aerogel while preserving its highly defective and porous structure.

MATERIALS AND METHODS

Reference Electrocatalyst

IrO_x benchmark was purchased from Surepure Chemetals and used as reference catalysts without further treatment.

IrCu Aerogel

This synthesis was modified from the work of Shi et al.[32] Typically, 193.5 mg of hexachloroiridate(IV) acid hydrate ($H_2IrCl_6{\cdot}xH_2O$, ≥99.995%, Sigma-Aldrich) and 21.3 mg of copper(II) chloride dihydrate ($CuCl_2{\cdot}2H_2O$, ≥99.95%, Sigma-Aldrich) were dissolved in 350 mL of Milli-Q water and stirred for 10 min. Subsequently, 57 mg of sodium borohydride ($NaBH_4$, ≥99%, Sigma-Aldrich), dissolved in 3 mL of Milli-Q water, was rapidly added under vigorous stirring. The solution was then left undisturbed in a water bath at 60 °C for approximately 5 h until the upper part becomes transparent. The resulting hydrogel was washed several times with Milli-Q water and freeze-dried overnight to obtain the final aerogel. The freeze-drying (lyophilization) process involved freezing the hydrogel in liquid nitrogen, followed by solvent sublimation under high vacuum (4×10^{-5} bar).

IrCu/C Nanoparticles

206 mg of $H_2IrCl_6{\cdot}xH_2O$ and 22.7 mg of $CuCl_2{\cdot}2H_2O$ were dissolved in 9 mL of absolute ethanol (AnalaR NORMAPUR, VWR Chemicals). Then, 159.6 mg of sodium hydroxide (NaOH, ≥98%, Sigma-Aldrich) was added under stirring. The solution was placed in an oil bath at 85 °C for 10 min. The color changed from yellow to green and then to light brown, indicating the formation of colloidal IrCu nanoparticles (NPs). The resulting NPs were mixed with Vulcan XC72 carbon to prepare a 20 wt % IrCu/C catalyst. The pH was adjusted to 1 by the dropwise addition of 1 M H_2SO_4. The carbon-supported IrCu nanoparticles were then filtered and dried at 80 °C for 3 h to obtain the final powder.

https://doi.org/10.1021/acscatal.5c07713
ACS Catal. 2026, 16, 4528−4540

High Energy X-ray Diffraction (XRD)

High energy XRD measurements were performed at the ID31 beamline of the European Synchrotron Radiation Facility (ESRF) in Grenoble, France. The high energy X-ray beam (75 keV) was used in different experimental configurations (*ex situ* and *in situ*) to investigate the structural properties of the electrocatalysts. The scattered signal was collected using a Dectris Pilatus 3X CdTe 2 M hybrid photocounting area detector. Extended details are provided in Supporting Information.

Electrochemical Measurements

Liquid-cell measurements were performed in a gas diffusion electrode (GDE) cell made of poly(tetrafluorethylene) (PTFE) (Gaskatel). An Ir loading of 50 $\mu g\ cm^{-2}$ was used. All measurements were conducted in a 1 M $HClO_4$ solution at room temperature.

Proton exchange membrane water electrolyzer (PEMWE) single-cell measurements were carried out using a membrane electrode assembly (MEA) composed of a catalyst-coated membrane (CCM) with an Ir loading of approximately 0.4 mg cm^{-2}, and a commercial GDE (cathode side) with a Pt/C loading of 0.5 mg cm^{-2}. Measurements were performed at 80 °C with a water flow rate of 200 mL min^{-1}. Extended details are provided in the Supporting Information.

Online-ICP-MS

A commercial electrochemical flow cell (BASi, MF-1092, cross-flow cell) was used. The flow cell consists of two glassy carbon disks (3 mm) aligned in series, which are embedded into PEEK housing. Electrocatalysts ink was deposited on a 0.071 cm^2 glassy carbon substrate to reach a Ir loading of 25 $\mu g_{Ir}\ cm^{-2}$. An Ag/AgCl reference electrode was used. The cell was fed with 1 M $HClO_4$ at a rate of 400 $\mu L\ min^{-1}$ using a peristaltic pump. Extended details are provided in the Supporting Information.

Ex Situ ICP-MS

An Agilent 7800 ICP-MS instrument equipped with a Micromist/Scott nebulizer was used. Ir-based catalysts were mineralized in aqua regia (3:1 mixture of HCl and HNO_3) using microwave-assisted digestion at 230 °C for 2 h with a heating ramp of 8 °C min^{-1}. Teflon reactors were used for the digestion.

High-Resolution Transmission Electron Microscopy (HR-TEM)

HR-TEM imaging of the catalysts was performed on a JEOL JEM-ARM200F Cold FEG instrument (probe-corrected) operated at 200 kV, achieving a point resolution higher than 1.9 Å. Experiments were conducted using both high-angle annular dark-field (HAADF) and bright-field (BF) detectors for optimal spatial resolution. The particle size distribution was determined by manually analyzing micrographs from multiple regions of the TEM grid, with at least 250 particles evaluated to ensure statistical relevance.

Energy-Dispersive X-ray Coupled with Scanning Electron Microscopy (EDX−SEM)

Cross-sectional EDX−SEM was performed using a Zeiss Sigma 300 field-emission scanning electron microscope (FE-SEM) equipped with secondary electron (SE) and five-segment backscattered electron (BSE) detectors. Elemental analyses were carried out using an Oxford Instruments X-Max SDD EDX detector operated with AZtec analysis software. The MEA was prepared by cryogenic fracture in liquid nitrogen in order to obtain a clean cross section.

Ex Situ X-ray Absorption Spectroscopy (XAS)

XAS measurements were conducted at the Ir L_3-edge (11.215 keV) using a Si(220) double-crystal monochromator in fluorescence mode with a 35-element Ge detector. Gas diffusion electrode (GDE) samples, prepared by drop-casting, as in the liquid-cell experiments, were analyzed at room temperature under ambient conditions. Data were processed with Athena software, and EXAFS spectra were extracted over a k-range of 3−12 $Å^{-1}$. The resulting $|\chi(R)|$ spectra were qualitatively compared in uncorrected R-space without a phase-shift correction or quantitative fitting. Extended details are provided in the Supporting Information.

Ex Situ X-ray Photoelectron Spectroscopy (XPS)

XPS measurements were performed by using a ThermoVG Multilab ESCA3000 spectrometer equipped with a RESOLVE 120 MCD5 hemispherical electron analyzer and a dual anode (Mg/Al) X-ray source. The Al Kα line (hv = 1486.6 eV) was used for the measurements. Survey, C 1s, and Ir 4f spectra were recorded, with the Ir 4f region acquired at a step size of 0.05 eV. Binding energies were calibrated to the C 1s peak at 284.6 eV. Extended details are provided in the Supporting Information.

■ ASSOCIATED CONTENT

Supporting Information

The Supporting Information is available free of charge at https://pubs.acs.org/doi/10.1021/acscatal.5c07713.

X-ray transparent thin-film electrochemical flow cell (Picture S1); GDE setup and its schematic representation (Picture S2); small-volume electrochemical flow cell used for online ICP-MS measurements (Picture S3); TEM images of the IrO_x Chemetals (Figure S1); fitted XPS spectra of the Ir 4f region for the different catalysts (Figure S2); TS-Rietveld microstructural parameters evolution during electrochemical activation of IrCu aerogel in 1 M $HClO_4$ (Figure S3); online ICP-MS dissolution profiles of Ir and Cu in 1 M $HClO_4$ during CV at 5 mV s^{-1} for IrCu aerogel, IrCu/C, and IrO_x Chemetals (Figure S4); online ICP-MS dissolution profiles of Ir and Cu in 1 M $HClO_4$ (Figure S5); total Cu loss after activation (Figure S6); Cu 2p XPS spectra of IrCu-based catalysts before and after electrochemical activation (Figure S7); *S*-number values for IrCu aerogel, IrCu/C, and IrO_x chemetals, calculated at 1.51 V *vs* RHE (Figure S8); *post mortem* dark-field HR-TEM (Figure S9); exemplary fits of the *in situ* TS-PDF experiments (Figure S10); exemplary $I(Q)$, $S(Q)$, $F(Q)$ and $G(r)$ from *in situ* data of the IrCu aerogel sample (Figure S11); microstructural parameters and chemical composition of the precatalysts by means of *ex situ* TS, ICP-MS, and TEM techniques (Table S1); elemental composition obtained from EDX spectra acquired at selected regions of the MEA cross section after continuous AST (Table S2); elemental composition obtained from EDX spectra collected from the anode catalyst layer of the MEA after continuous AST (Table S3) (DOCX)

■ AUTHOR INFORMATION

Corresponding Authors

Amir Gasmi − *ICGM, Univ. Montpellier, CNRS, ENSCM, 34095 Montpellier, France;* orcid.org/0000-0001-9433-9432; Email: amir.gasmi@umontpellier.fr

Raphaël Chattot − *ICGM, Univ. Montpellier, CNRS, ENSCM, 34095 Montpellier, France;* orcid.org/0000-0001-6169-530X; Email: raphael.chattot@umontpellier.fr

Authors

Meryem Ennaji − *ICGM, Univ. Montpellier, CNRS, ENSCM, 34095 Montpellier, France*

Carlos A. Campos-Roldán − *ICGM, Univ. Montpellier, CNRS, ENSCM, 34095 Montpellier, France;* orcid.org/0000-0002-1517-9037

https://doi.org/10.1021/acscatal.5c07713
ACS Catal. 2026, 16, 4528−4540

Morgane Stodel − *CIRIMAT, Université de Toulouse, CNRS, UT3 Paul Sabatier, 31062 Toulouse, France*
Tristan Asset − *ICPEES, UMR 7515 CNRS-ECPM-Université de Strasbourg, 67087 Strasbourg, France*
Vasiliki Papaefthymiou − *ICPEES, UMR 7515 CNRS-ECPM-Université de Strasbourg, 67087 Strasbourg, France*
Andrea Zitolo − *Synchrotron SOLEIL, L'orme des Merisiers, 91192 Gif-sur-Yvette, France;* orcid.org/0000-0002-2187-6699
Marc Dupont − *ICGM, Univ. Montpellier, CNRS, ENSCM, 34095 Montpellier, France*
Frédéric Lecoeur − *ICGM, Univ. Montpellier, CNRS, ENSCM, 34095 Montpellier, France*
Jakub Drnec − *ESRF, The European Synchrotron, 38043 Grenoble, France*
Deborah Jones − *ICGM, Univ. Montpellier, CNRS, ENSCM, 34095 Montpellier, France*

Complete contact information is available at: https://pubs.acs.org/10.1021/acscatal.5c07713

Notes

The authors declare no competing financial interest.

■ ACKNOWLEDGMENTS

The authors thank the ESRF for providing beamtime at ID31 under proposal number CH6721. The authors acknowledge the Balard Analysis and Characterization Platform (PAC Balard) facilities for technical support, and especially thank M. Bigot for his valuable help with the ICP-MS setup. R.C gratefully acknowledges financial support from the French National Research Agency through the HOLYCAT project (grant number no. ANR-22-CE05-0007).

■ REFERENCES

(1) Renewables now (REN21). Renewables 2019 Global Status Report, 2019. https://www.ren21.net/reports/global-status-report/ (accessed Dec 31, 2025).
(2) Abe, J. O.; Popoola, A. P. I.; Ajenifuja, E.; Popoola, O. M. Hydrogen Energy, Economy and Storage: Review and Recommendation. *Int. J. Hydrogen Energy* **2019**, *44* (29), 15072−15086.
(3) da Silva Veras, T.; Mozer, T. S.; da Costa Rubim Messeder dos Santos, D.; da Silva César, A. Hydrogen: Trends, Production and Characterization of the Main Process Worldwide. *Int. J. Hydrogen Energy* **2017**, *42* (4), 2018−2033.
(4) Dincer, I.; Acar, C. Smart Energy Solutions with Hydrogen Options. *Int. J. Hydrogen Energy* **2018**, *43* (18), 8579−8599.
(5) Trattner, A.; Klell, M.; Radner, F. Sustainable Hydrogen Society − Vision, Findings and Development of a Hydrogen Economy Using the Example of Austria. *Int. J. Hydrogen Energy* **2022**, *47* (4), 2059−2079.
(6) Rizwan, M.; Alstad, V.; Jäschke, J. Design Considerations for Industrial Water Electrolyzer Plants. *Int. J. Hydrogen Energy* **2021**, *46* (75), 37120−37136.
(7) Makhsoos, A.; Kandidayeni, M.; Boulon, L.; Pollet, B. G. A Comparative Analysis of Single and Modular Proton Exchange Membrane Water Electrolyzers for Green Hydrogen Production- a Case Study in Trois-Rivières. *Energy* **2023**, *282*, No. 128911.
(8) Hydrogen Europe. EU's Third Hydrogen Bank Auction to Partially Open to Low-Carbon Electrolytic Hydrogen with €1.1bn Budget, 2024. https://hydrogeneurope.eu/eus-third-hydrogen-bank-auction-to-partially-open-to-low-carbon-electrolytic-hydrogen-with-e1-1bn-budget/ (accessed Dec 31, 2025).
(9) Sapountzi, F. M.; Gracia, J. M.; Weststrate, C. J.; Fredriksson, H. O. A.; Niemantsverdriet, J. W. Electrocatalysts for the Generation of Hydrogen, Oxygen and Synthesis Gas. *Prog. Energy Combust. Sci.* **2017**, *58*, 1−35.
(10) Bertuccioli, L.; Chan, A.; Hart, D.; Lehner, F.; Madden, B.; Standen, E. Development of Water Electrolysis in the European Union; Brussels, 2014. https://www.clean-hydrogen.europa.eu/media/publications/development-water-electrolysis-european-union_en (accessed Dec 31, 2025).
(11) Schmidt, O.; Gambhir, A.; Staffell, I.; Hawkes, A.; Nelson, J.; Few, S. Future Cost and Performance of Water Electrolysis: An Expert Elicitation Study. *Int. J. Hydrogen Energy* **2017**, *42* (52), 30470−30492.
(12) Feng, Q.; Yuan, X.; Liu, G.; Wei, B.; Zhang, Z.; Li, H.; Wang, H. A Review of Proton Exchange Membrane Water Electrolysis on Degradation Mechanisms and Mitigation Strategies. *J. Power Sources* **2017**, *366*, 33−55.
(13) Mittelsteadt, C.; Sorensen, E.; Jia, Q. Ir Strangelove, or How to Learn to Stop Worrying and Love the PEM Water Electrolysis. *Energy Fuels* **2023**, *37* (17), 12558−12569.
(14) Clapp, M.; Zalitis, C. M.; Ryan, M. Perspectives on Current and Future Iridium Demand and Iridium Oxide Catalysts for PEM Water Electrolysis. *Catal. Today* **2023**, *420*, No. 114140.
(15) Ayers, K.; Danilovic, N.; Ouimet, R.; Carmo, M.; Pivovar, B.; Bornstein, M. Perspectives on Low-Temperature Electrolysis and Potential for Renewable Hydrogen at Scale. *Annu. Rev. Chem. Biomol Eng.* **2019**, *10* (1), 219−239.
(16) Kumar, S. S.; Kumar, A.; Malyan, S. K.; Ghosh, P.; Kumar, M.; Kapoor, R.; Agrawal, A. K.; Kumar, S.; Kumar, V.; Singh, L. Landfill Leachate Valorization: A Potential Alternative to Burden off Resources and Support Energy Systems. *Fuel* **2023**, *331*, No. 125911.
(17) Möckl, M.; Ernst, M. F.; Kornherr, M.; Allebrod, F.; Bernt, M.; Byrknes, J.; Eickes, C.; Gebauer, C.; Moskovtseva, A.; Gasteiger, H. A. Durability Testing of Low-Iridium PEM Water Electrolysis Membrane Electrode Assemblies. *J. Electrochem. Soc.* **2022**, *169* (6), No. 064505.
(18) Reier, T.; Oezaslan, M.; Strasser, P. Electrocatalytic Oxygen Evolution Reaction (OER) on Ru, Ir, and Pt Catalysts: A Comparative Study of Nanoparticles and Bulk Materials. *ACS Catal.* **2012**, *2* (8), 1765−1772.
(19) Nørskov, J. K.; Bligaard, T.; Rossmeisl, J.; Christensen, C. H. Towards the Computational Design of Solid Catalysts. *Nat. Chem.* **2009**, *1* (1), 37−46.
(20) Moriau, L.; Smiljanić, M.; Lončar, A.; Hodnik, N. Supported Iridium-based Oxygen Evolution Reaction Electrocatalysts - Recent Developments. *ChemCatChem* **2022**, *14* (20), No. e202200586, DOI: 10.1002/cctc.202200586.
(21) Wang, C.; Lan, F.; He, Z.; Xie, X.; Zhao, Y.; Hou, H.; Guo, L.; Murugadoss, V.; Liu, H.; Shao, Q.; Gao, Q.; Ding, T.; Wei, R.; Guo, Z. Iridium-Based Catalysts for Solid Polymer Electrolyte Electrocatalytic Water Splitting. *ChemSusChem* **2019**, *12* (8), 1576−1590.
(22) Oh, H.-S.; Nong, H. N.; Reier, T.; Bergmann, A.; Gliech, M.; Ferreira de Araújo, J.; Willinger, E.; Schlögl, R.; Teschner, D.; Strasser, P. Electrochemical Catalyst−Support Effects and Their Stabilizing Role for IrO *x* Nanoparticle Catalysts during the Oxygen Evolution Reaction. *J. Am. Chem. Soc.* **2016**, *138* (38), 12552−12563.
(23) Nong, H. N.; Oh, H.; Reier, T.; Willinger, E.; Willinger, M.; Petkov, V.; Teschner, D.; Strasser, P. Oxide-Supported $IrNiO_x$ Core−Shell Particles as Efficient, Cost-Effective, and Stable Catalysts for Electrochemical Water Splitting. *Angew. Chem., Int. Ed.* **2015**, *54* (10), 2975−2979.
(24) Oh, H.-S.; Nong, H. N.; Reier, T.; Gliech, M.; Strasser, P. Oxide-Supported Ir Nanodendrites with High Activity and Durability for the Oxygen Evolution Reaction in Acid PEM Water Electrolyzers. *Chem. Sci.* **2015**, *6* (6), 3321−3328.
(25) Oh, H. S.; Nong, H. N.; Strasser, P. Preparation of Mesoporous Sb-, F-, and in-Doped SnO2 Bulk Powder with High Surface Area for Use as Catalyst Supports in Electrolytic Cells. *Adv. Funct Mater.* **2015**, *25* (7), 1074−1081.
(26) Daiane Ferreira da Silva, C.; Claudel, F.; Martin, V.; Chattot, R.; Abbou, S.; Kumar, K.; Jiménez-Morales, I.; Cavaliere, S.; Jones, D.;

Rozière, J.; Solà-Hernandez, L.; Beauger, C.; Faustini, M.; Peron, J.; Gilles, B.; Encinas, T.; Piccolo, L.; Barros de Lima, F. H.; Dubau, L.; Maillard, F. Oxygen Evolution Reaction Activity and Stability Benchmarks for Supported and Unsupported IrO_x Electrocatalysts. *ACS Catal.* **2021**, *11* (7), 4107−4116.
(27) Jiménez-Morales, I.; Rozière, J.; Jones, D.; Cavaliere, S. A Comprehensive Activity−Stability Correlation Study of Tantalum-Doped Tin Oxide as a Support for Iridium Oxide in Low Loading Water Electrolysis Cell Anodes. *RSC Appl. Interfaces* **2025**, *2*, 965.
(28) Tran, H. P.; Nong, H. N.; Oh, H.-S.; Klingenhof, M.; Kroschel, M.; Paul, B.; Hübner, J.; Teschner, D.; Strasser, P. Catalyst−Support Surface Charge Effects on Structure and Activity of IrNi-Based Oxygen Evolution Reaction Catalysts Deposited on Tin-Oxide Supports. *Chem. Mater.* **2022**, *34* (21), 9350−9363.
(29) Solà-Hernández, L.; Claudel, F.; Maillard, F.; Beauger, C. Doped Tin Oxide Aerogels as Oxygen Evolution Reaction Catalyst Supports. *Int. J. Hydrogen Energy* **2019**, *44* (45), 24331−24341.
(30) Abbou, S.; Chattot, R.; Martin, V.; Claudel, F.; Solà-Hernandez, L.; Beauger, C.; Dubau, L.; Maillard, F. Manipulating the Corrosion Resistance of SnO_2 Aerogels through Doping for Efficient and Durable Oxygen Evolution Reaction Electrocatalysis in Acidic Media. *ACS Catal.* **2020**, *10* (13), 7283−7294.
(31) Jiménez-Morales, I.; Cavaliere, S.; Dupont, M.; Jones, D.; Rozière, J. On the Stability of Antimony Doped Tin Oxide Supports in Proton Exchange Membrane Fuel Cell and Water Electrolysers. *Sustainable Energy Fuels* **2019**, *3* (6), 1526−1535.
(32) Shi, Q.; Zhu, C.; Zhong, H.; Su, D.; Li, N.; Engelhard, M. H.; Xia, H.; Zhang, Q.; Feng, S.; Beckman, S. P.; Du, D.; Lin, Y. Nanovoid Incorporated Ir_xCu Metallic Aerogels for Oxygen Evolution Reaction Catalysis. *ACS Energy Lett.* **2018**, *3* (9), 2038−2044.
(33) Cai, B.; Eychmüller, A. Promoting Electrocatalysis upon Aerogels. *Adv. Mater.* **2019**, *31* (31), No. 1804881, DOI: 10.1002/adma.201804881.
(34) Calle-Vallejo, F.; Pohl, M. D.; Bandarenka, A. S. Quantitative Coordination−Activity Relations for the Design of Enhanced Pt Catalysts for CO Electro-Oxidation. *ACS Catal.* **2017**, *7* (7), 4355−4359.
(35) Calle-Vallejo, F.; Pohl, M. D.; Reinisch, D.; Loffreda, D.; Sautet, P.; Bandarenka, A. S. Why Conclusions from Platinum Model Surfaces Do Not Necessarily Lead to Enhanced Nanoparticle Catalysts for the Oxygen Reduction Reaction. *Chem. Sci.* **2017**, *8* (3), 2283−2289.
(36) Calle-Vallejo, F.; Tymoczko, J.; Colic, V.; Vu, Q. H.; Pohl, M. D.; Morgenstern, K.; Loffreda, D.; Sautet, P.; Schuhmann, W.; Bandarenka, A. S. Finding Optimal Surface Sites on Heterogeneous Catalysts by Counting Nearest Neighbors. *Science* **2015**, *350* (6257), 185−189.
(37) Dubau, L.; Nelayah, J.; Moldovan, S.; Ersen, O.; Bordet, P.; Drnec, J.; Asset, T.; Chattot, R.; Maillard, F. Defects Do Catalysis: CO Monolayer Oxidation and Oxygen Reduction Reaction on Hollow PtNi/C Nanoparticles. *ACS Catal.* **2016**, *6* (7), 4673−4684.
(38) Chattot, R.; Asset, T.; Bordet, P.; Drnec, J.; Dubau, L.; Maillard, F. Beyond Strain and Ligand Effects: Microstrain-Induced Enhancement of the Oxygen Reduction Reaction Kinetics on Various PtNi/C Nanostructures. *ACS Catal.* **2017**, *7* (1), 398−408.
(39) Chattot, R.; Le Bacq, O.; Beermann, V.; Kühl, S.; Herranz, J.; Henning, S.; Kühn, L.; Asset, T.; Guétaz, L.; Renou, G.; Drnec, J.; Bordet, P.; Pasturel, A.; Eychmüller, A.; Schmidt, T. J.; Strasser, P.; Dubau, L.; Maillard, F. Surface Distortion as a Unifying Concept and Descriptor in Oxygen Reduction Reaction Electrocatalysis. *Nat. Mater.* **2018**, *17* (9), 827−833.
(40) Bu, L.; Zhang, N.; Guo, S.; Zhang, X.; Li, J.; Yao, J.; Wu, T.; Lu, G.; Ma, J.-Y.; Su, D.; Huang, X. Biaxially Strained PtPb/Pt Core/Shell Nanoplate Boosts Oxygen Reduction Catalysis. *Science* **2016**, *354* (6318), 1410−1414.
(41) Asset, T.; Chattot, R.; Drnec, J.; Bordet, P.; Job, N.; Maillard, F.; Dubau, L. Elucidating the Mechanisms Driving the Aging of Porous Hollow PtNi/C Nanoparticles by Means of CO_ad_s Stripping. *ACS Appl. Mater. Interfaces* **2017**, *9* (30), 25298−25307.
(42) Le Bacq, O.; Pasturel, A.; Chattot, R.; Previdello, B.; Nelayah, J.; Asset, T.; Dubau, L.; Maillard, F. Effect of Atomic Vacancies on the Structure and the Electrocatalytic Activity of Pt-rich/C Nanoparticles: A Combined Experimental and Density Functional Theory Study. *ChemCatChem* **2017**, *9* (12), 2324−2338.
(43) Hofer, E. M.; Hintermann, H. E. Correlation between the Catalytic Activity of Raney Nickel and Its Structure. *Trans. Faraday Soc.* **1964**, *60*, 1457.
(44) Dubau, L.; Nelayah, J.; Asset, T.; Chattot, R.; Maillard, F. Implementing Structural Disorder as a Promising Direction for Improving the Stability of PtNi/C Nanoparticles. *ACS Catal.* **2017**, *7* (4), 3072−3081.
(45) Chattot, R.; Bordet, P.; Martens, I.; Drnec, J.; Dubau, L.; Maillard, F. Building Practical Descriptors for Defect Engineering of Electrocatalytic Materials. *ACS Catal.* **2020**, *10* (16), 9046−9056.
(46) Wang, J.-Q.; Xi, C.; Wang, M.; Shang, L.; Mao, J.; Dong, C.-K.; Liu, H.; Kulinich, S. A.; Du, X.-W. Laser-Generated Grain Boundaries in Ruthenium Nanoparticles for Boosting Oxygen Evolution Reaction. *ACS Catal.* **2020**, *10* (21), 12575−12581.
(47) Bornet, A.; Pittkowski, R.; Nielsen, T. M.; Berner, E.; Maletzko, A.; Schröder, J.; Quinson, J.; Melke, J.; Jensen, K. M. Ø.; Arenz, M. Influence of Temperature on the Performance of Carbon- and ATO-Supported Oxygen Evolution Reaction Catalysts in a Gas Diffusion Electrode Setup. *ACS Catal.* **2023**, *13* (11), 7568−7577.
(48) Pittkowski, R. K.; Punke, S.; Anker, A. S.; Bornet, A.; Magnard, N. P. L.; Schlegel, N.; Graversen, L. G.; Quinson, J.; Dworzak, A.; Oezaslan, M.; Kirkensgaard, J. J. K.; Mirolo, M.; Drnec, J.; Arenz, M.; Jensen, K. M. Ø. Monitoring the Structural Changes in Iridium Nanoparticles during Oxygen Evolution Electrocatalysis with *Operando* X-Ray Total Scattering. *J. Am. Chem. Soc.* **2024**, *146* (40), 27517−27527.
(49) Pfeifer, V.; Jones, T. E.; Velasco Vélez, J. J.; Arrigo, R.; Piccinin, S.; Hävecker, M.; Knop-Gericke, A.; Schlögl, R. In Situ Observation of Reactive Oxygen Species Forming on Oxygen-Evolving Iridium Surfaces. *Chem. Sci.* **2017**, *8* (3), 2143−2149.
(50) Campos-Roldán, C. A.; Gasmi, A.; Ennaji, M.; Stodel, M.; Martens, I.; Filhol, J.-S.; Blanchard, P.-Y.; Cavaliere, S.; Jones, D.; Drnec, J.; Chattot, R. Metal-Oxide Phase Transition of Platinum Nanocatalyst below Fuel Cell Open-Circuit Voltage. *Nat. Commun.* **2025**, *16* (1), No. 936.
(51) Chattot, R.; Martens, I.; Mirolo, M.; Ronovsky, M.; Russello, F.; Isern, H.; Braesch, G.; Hornberger, E.; Strasser, P.; Sibert, E.; Chatenet, M.; Honkimäki, V.; Drnec, J. Electrochemical Strain Dynamics in Noble Metal Nanocatalysts. *J. Am. Chem. Soc.* **2021**, *143* (41), 17068−17078.
(52) Jovanovič, P.; Hodnik, N.; Ruiz-Zepeda, F.; Arčon, I.; Jozinović, B.; Zorko, M.; Bele, M.; Šala, M.; Šelih, V. S.; Hočevar, S.; Gaberščck, M. Electrochemical Dissolution of Iridium and Iridium Oxide Particles in Acidic Media: Transmission Electron Microscopy, Electrochemical Flow Cell Coupled to Inductively Coupled Plasma Mass Spectrometry, and X-Ray Absorption Spectroscopy Study. *J. Am. Chem. Soc.* **2017**, *139* (36), 12837−12846.
(53) Clauss, D.; Martin, V.; Nelayah, J.; Chattot, R.; Bordet, P.; Drnec, J.; Mirolo, M.; Dubau, L.; Maillard, F. A Model Approach to Uncover the Role of the IrOx Crystallographic Structure and Chemistry on OER Activity and Stability via Annealing a Sacrificial Template. *ACS Catal.* **2025**, *15*, 2654−2665.
(54) Cheng, Z.; Huang, B.; Pi, Y.; Li, L.; Shao, Q.; Huang, X. Partially Hydroxylated Ultrathin Iridium Nanosheets as Efficient Electrocatalysts for Water Splitting. *Natl. Sci. Rev.* **2020**, *7* (8), 1340−1348.
(55) Liu, H.; Wang, X.; Lao, K.; Wen, L.; Huang, M.; Liu, J.; Hu, T.; Hu, B.; Xie, S.; Li, S.; Fang, X.; Zheng, N.; Tao, H. B. Optimizing Ionomer Distribution in Anode Catalyst Layer for Stable Proton Exchange Membrane Water Electrolysis. *Adv. Mater.* **2024**, *36* (28), No. 2402780, DOI: 10.1002/adma.202402780.
(56) Yuan, S.; Zhao, C.; Luo, L.; Fu, C.; Li, H.; An, L.; Cheng, X.; Shen, S.; Yin, J.; Yan, X.; Zhang, J. Revealing the Role of the Ionomer

at the Triple-Phase Boundary in a Proton-Exchange Membrane Water Electrolyzer. *J. Phys. Chem. Lett.* **2024**, *15* (19), 5223−5230.
(57) Bernt, M.; Hartig-Weiß, A.; Tovini, M. F.; El-Sayed, H. A.; Schramm, C.; Schröter, J.; Gebauer, C.; Gasteiger, H. A. Current Challenges in Catalyst Development for PEM Water Electrolyzers. *Chem. Ing. Tech.* **2020**, *92* (1−2), 31−39.
(58) Geiger, S.; Kasian, O.; Ledendecker, M.; Pizzutilo, E.; Mingers, A. M.; Fu, W. T.; Diaz-Morales, O.; Li, Z.; Oellers, T.; Fruchter, L.; Ludwig, A.; Mayrhofer, K. J. J.; Koper, M. T. M.; Cherevko, S. The Stability Number as a Metric for Electrocatalyst Stability Benchmarking. *Nat. Catal.* **2018**, *1* (7), 508−515.
(59) Lončar, A.; Escalera-López, D.; Cherevko, S.; Hodnik, N. Interrelationships between Oxygen Evolution and Iridium Dissolution Mechanisms. *Angew. Chem., Int. Ed.* **2022**, *61* (14), No. e202114437, DOI: 10.1002/anie.202114437.
(60) Weiß, A.; Siebel, A.; Bernt, M.; Shen, T.-H.; Tileli, V.; Gasteiger, H. A. Impact of Intermittent Operation on Lifetime and Performance of a PEM Water Electrolyzer. *J. Electrochem. Soc.* **2019**, *166* (8), F487−F497.

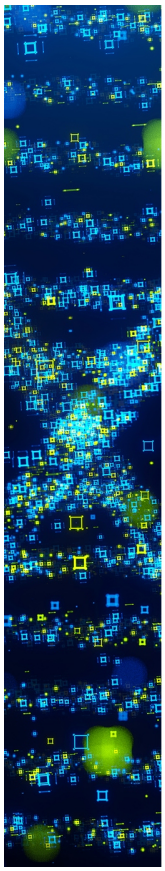
CAS BIOFINDER DISCOVERY PLATFORM™
STOP DIGGING THROUGH DATA —START MAKING DISCOVERIES
CAS BioFinder helps you find the right biological insights in seconds
Start your search
CAS
A division of the American Chemical Society

https://doi.org/10.1021/acscatal.5c07713
ACS Catal. 2026, 16, 4528−4540